Applied Composite Materials
https://doi.org/10.1007/s10443-021-10000-5

Experimental Investigation of the Interlaminar Failure of Glass/Elium® Thermoplastic Composites Manufactured With Different Processing Temperatures

Ning Han[1] · Onur Yuksel[2] · Jamal Seyyed Monfared Zanjani[2] · LuLing An[3] · Remko Akkerman[2] · Ismet Baran[2]

Received: 17 June 2021 / Accepted: 22 November 2021

Abstract
The aim of this study is to evaluate the effect of the processing temperature on the interfacial failure of glass/Elium® 150 composites. The vacuum assisted resin transfer molding technique (VARTM) was used to manufacture glass/Elium® 150 composites at three different process temperatures: room temperature (24℃), 50℃ and 80℃. The interlaminar shear strength, mode I and mode II interlaminar fracture toughness of the laminates were determined by performing the short beam shear (SBS), double cantilever beam (DCB) and end notched flexure (ENF) tests, respectively. It was found that the increase in processing temperature improved the interlaminar shear strength, mode I and mode II interlaminar fracture toughness by approximately 41%, 66% and 227%, respectively. A combined compressive and shear failure mode was found in SBS tests. Fiber bridging was present for all the composite specimens in DCB tests according to the travelling recording camera images. Fracture surface images obtained by scanning electron microscopy (SEM) after the ENF tests revealed that a better fiber-matrix bonding and a ductile matrix failure were obtained for higher processing temperatures.

Keywords Thermoplastic composites (TPCs) · Interlaminar fracture · Fracture toughness · Vacuum assisted resin transfer molding (VARTM) · Glass/Elium · Scanning electron microscopy (SEM)

✉ LuLing An
anllme@nuaa.edu.cn

✉ Ismet Baran
i.baran@utwente.nl

Ning Han
hanning@nuaa.edu.cn

[1] School of Mechanical Engineering, Changzhou University, Changzhou 213164, China

[2] Faculty of Engineering Technology, University of Twente, NL-7500AE Enschede, Netherlands

[3] College of Mechanical & Electrical Engineering, Nanjing University of Aeronautics and Astronautics, Nanjing 210016, China

Published online: 03 January 2022

1 Introduction

Fiber reinforced thermoplastic composites (FRTPCs) have grown rapidly in several industries due to their outstanding character of recyclability and reprocessibility besides their high strength-to-weigh tratio [1, 2]. In addition, FRTPCs have high impact resistance with high fracture toughness which make them suitable for damage resistant applications. However, the manufacturing of FRTPCs is limited mainly due to the high melt viscosity of the thermoplastic polymer matrix which makes the impregnation of the fibers more difficult. Alternative to thermoplastic polymers, thermoplastic monomers which are viscous at room temperature due to their shorter chains can be used to impregnate the fiber reinforcement during the manufacturing processes of FRTPCs such as vacuum infusion, resin transfer molding and pultrusion. An example is the Elium® resin recently developed by Arkema which is based on an acrylic thermoplastic. The Elium® resin consists of 2-Propenoic acid, 2-methyl-, methyl ester or methylmethacrylate monomer (MMA) and acrylic copolymers in which MMA undergoes a free radical polymerization to its polymer PMMA [3]. This polymerization makes it possible to process the liquid thermoplastic Elium® resins similar to conventional thermosetting resins [4, 5], e.g. infusing them at room temperature.

Fiber reinforced Elium® composites (FRECs) have still been under development by using various manufacturing techniques such as vacuum assisted resin transfer molding (VARTM) [6, 7] and pultrusion [8]. Therefore, material characterization and a better understanding of the processing conditions, as well as mechanical performance are required to utilized FRECs in industrial applications. The mechanical performance of recently developed Elium® composites with different fiber reinforcement types has been investigated in the literature such as the impact response [9–12], flexure strength [13, 14], tensile strength [14–16], fatigue behaviour [17, 18] and indentation response [19, 20]. In addition, there have been studies dealing with the characterization of the interlaminar mechanical properties such as interlaminar shear strength (ILSS), mode-I fracture toughness (G_C) and mode-II fracture toughness (G_{IIC}) of FRECs. Since the focus of this paper is on the interlaminar failure behavior of FRECs, these studies are summarized in Table 1. It is seen that the experimentally determined ILSS of FRECs by using the short beam shear (SBS) tests varied between approximately 40 MPa and 58 MPa [5, 21–24]. Double cantilevered beam (DCB) tests were performed to determine G_{IC} of FRECs and the range of G_{IC} was found to be from approximately 1.0 kJ/m^2 to 2.5 kJ/m^2 [5, 7, 24–26]. The mode-II fracture toughness of a FREC was determined in Barbosa et al. [27] by using the end notched failure (ENF) test and G_{IIC} was found to be approximately 1.3 kJ/m^2.

Although there have been several studies carried out to quantify the mechanical properties and performance, a critical assessment of the effect of processing temperature on the interlaminar failure behavior of FRECs needs to be addressed to develop future's high damage tolerant FRECs. The manufacturing process has a direct influence on the material properties of the final product such as fracture toughness, degree of cure, degree of crystallinity, elastic modulus and strength [28–30]. The mechanical properties of Elium® resins are also directly influenced by the processing temperature and initiator percentage, which affect the final degree of the polymerization as studied in [31, 32].

To date and for the best of the authors' knowledge, the interlaminar failure behavior of Elium® composite manufacturing under different processing temperatures has not been addressed as seen in Table 1. The present work critically evaluates the influence of processing temperature on the interlaminar failure behavior of unidirectional glass fiber reinforced Elium® composites manufactured by VARTM. Three processing temperatures were used

Table 1 Summary of the studies focusing on interlaminar failure behavior of fiber reinforced Elium® composites manufactured by using the VARTM method in literatures

Reference	Material		Test	Value	Processing temperature in VARTM
	Reinforcement	Matrix			
Barbosa et al. [27]	The 0/90° plain weave carbon fabric	Elium 150	ENF	$G_{IIC} = 1.3$ kJ/m^2	25 ℃
Pini et al. [25]	UD carbon fibres	Elium	DCB	$G_{IC} = 1.0$ kJ/m^2	RT** and post-curing at 80 °C and 120 °C
		Elium Impact		$G_{IC} = 2.51$ kJ/m^2	80 °C and post-curing at 125 °C
Shanmugam et al. [7]	plain-woven UHMWPE* fabric	Elium 188	DCB	$G_{IC} = 2.09$ kJ/m^2	RT**
Obande et al. [5]	UD glass fabric	Elium 188	SBS	ILSS = 58 MPa	RT**
			DCB	$G_{IC} = 1.814$ kJ/m^2	
Nash et al. [21]	UD glass fabric	Elium 150	SBS	ILSS = 56.9 MPa	25 ℃
Bhudolia et al. [22]	Carbon fabric	Elium 280	SBS	ILSS = 45 MPa	RT** and post-curing at 80 °C
Davies and Arhant [23]	Carbon fabric	Elium 180	SBS	ILSS = 40.2 MPa	RT** and post-curing at 65 °C
	E-glass fabric			ILSS = 46 MPa	
Mamalis et al. [24]	UD E-glass fabric	Elium180	SBS	ILSS = 40 MPa	unknown
			DCB	$G_{IC} = 2.1$ kJ/m^2	
Bhudolia [26]	carbon fabric	Elium 280	DCB	$G_{IC} = 1.6$ kJ/m^2	RT**and post-curing at 80 °C

UHMWPE: ultra-high-molecular-weight polyethylene

**RT:* Room temperature

to produce specimens for SBS, DCB and ENF tests. The temperature evolution was monitored for each glass/Elium® laminate and the microstructure of the manufactured laminates was analyzed by an optical light microscopy. The failure evolution during SBS and DCB tests was recorded by using a camera. Scanning electron microscope (SEM) was utilized to describe the damage and fracture mechanisms after the ENF tests.

The following section describes the materials and processing techniques used in detail. Section 3 presents the description of the mechanical tests employed to quantify the ILSS, G_{IC} and G_{IIC}. The obtained results are presented in Sect. 4 and discussed in Sect. 5. Finally, the conclusions and recommendations for future work are presented in Sect. 6.

2 Materials and Processing

2.1 Materials

The laminated composites were made of unidirectional (UD) glass fiber reinforced Elium 150 resin (Arkema, France). The viscosity and liquid density of Elium 150 resin were 0.1 Pa·s and 1.01 g/m^3, respectively [12]. In order to initiate the polymerization reaction of the Elium 150 resin during the VARTM process, Perkadox CH-50X initiator (2% by weight) was used according to the resin manufacturer's datasheet. The UD E-glass fabric with an areal weight of 750gsm (consisting of 660 gsm roving and 90 gsm random filament as stitching) was used as the fiber reinforcement.

2.2 Manufacturing of Elium Composites

Figure 1 shows the vacuum assisted resin infusion process setup. Glass/Elium 150 laminates were prepared by using the VARTM [33]. A total of four layers of fabric were firstly placed on the glass mold which was waxed with the 227-CEE release agent. A teflon film covered with release agent was subsequently placed between the second and third layers of the composite to introduce an initial delamination as shown in Fig. 1(a). The thickness, width and length of the teflon tape were approximately 13 µm, 60 mm and 300 mm, respectively. The structure of the top surface of fabric consisted of glass fiber bundles and knitted stitching fibers that were used to align the fiber bundles as seen in Fig. 1(b). On the

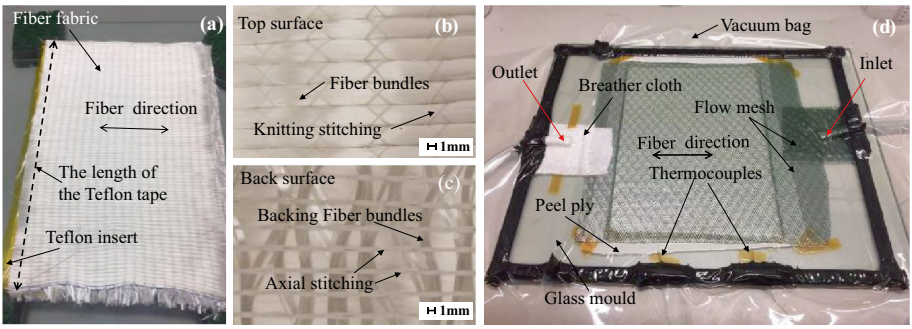

Fig. 1 The vacuum assisted resin infusion process setup. (**a**) The UD glass fabric and teflon tape. (**b**) The structure of top surface fabric. (**c**) The structure of back surface fabric. (**d**) The configuration of VARTM experiment

other hand, backing fiber bundles and axial stitching fibers were used for the back surface of the fabric as seen in Fig. 1(c) in order to keep the UD fabric in place. Two thermocouples were placed at the middle of the laminate to measure the temperature evolution during the process. Afterward, the peel ply, flow mesh and vacuum bag were placed. The breather cloth was put in the outlet location to absorb the surplus and reverse-flowing resin. The resin mixture (Elium 150 resin + Perkadox CH-50X initiator) was stirred for 2 min and afterward degassed for 2 min before the VARTM process. It is worth noting that the whole experimental setup was placed in an oven after infusing the resin mixture at room temperature (24 ℃). A total of three laminates was prepared under the same procedure with different isothermal polymerization temperatures: i) at room temperature (24 ℃), ii) 50℃ and iii) 80 ℃, which were denoted as RT, 50C and 80C laminate, respectively. The maximum processing temperature was determined as 80℃ in order to prevent part temperature being larger than the boiling temperature of Elium resin (~ 100 ℃) due to exothermic polymerization reaction as studied in [29].

The schematic view of the laminate configuration is shown in Fig. 2. The width and length of RT, 50C and 80C laminate were approximately 220 mm and 300 mm, respectively. The nominal thickness of the laminates after the manufacturing process was 3.8 mm ± 0.2 mm, i.e. each ply had approximately a nominal thickness of 0.95 mm. This corresponded to a nominal fiber volume content of 55% ± 2%. To avoid interlaminar defects caused by the inserted thermocouples, specimens were machined along the sides denotes as the dashed lines in Fig. 2 before the mechanical tests. The length and width of the trimmed laminates were approximately 250 mm and 200 mm, respectively. The width of Teflon in the trimmed laminate was 55 mm ± 2 mm. The positions of the thermocouples are also indicated in Fig. 2 and the side view of the laminate is shown in Fig. 2(b). The cross-sections of RT, 50C and 80C laminate were analyzed under a digital microscope (Keyene VHX) to assess the quality of the manufactured composites. Three specimens were cut from different positions of each laminate to calculate the void content of its cross section. And the average void content value of these three specimens was assumed to be the void content of the entire laminate.

3 Mechanical Testing

3.1 Short Beam Shear Test

The short beam shear (SBS) test was designed by using a three point bending setup to characterize the interlaminar shear strength (ILSS) of the manufactured laminates. The three-point short beam bending test was performed by using the Zwick/Roell Z5.0 testing machine at room temperature. Figure 3(a) shows the SBS test setup and the specimen configuration. A Nikon D5600 camera (frame rate of 60 fps, shutter of 120 1/s) was used to record the failure process of specimens in time during the SBS tests. The failure characterization of specimens was detected and observed clearly by using magnifying machine during the test process. The fractured SBS specimens were analyzed by Keyence VHX digital microscope to describe failure types after the test.

The specimen was loaded by a loading nose with 3 mm radius which was located at the center of the span as seen in Fig. 3(b). It was fixed by two supports which had rounded tips with a radius of 1.5 mm. The displacement speed was set to 1 mm/min. A total of five SBS specimens was prepared for each RT, 50C and 80C test, i.e. total of 15 SBS tests.

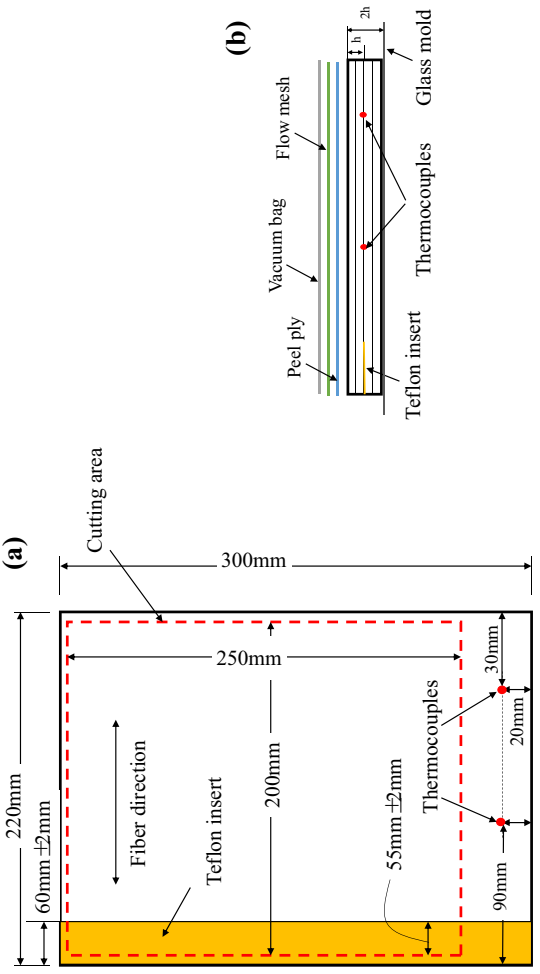

Fig. 2 The laminate configuration. (**a**) Top view. (**b**) Side view

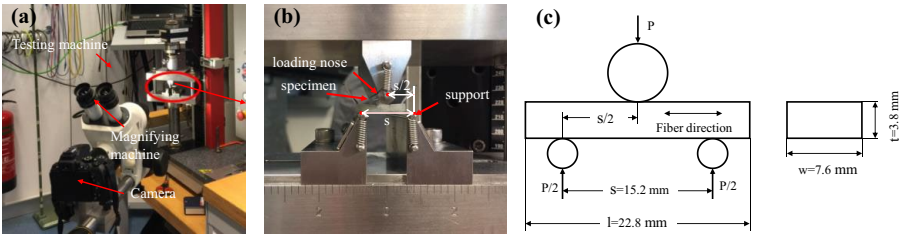

Fig. 3 (**a**) The experimental setup of the three point bending test, (**b**) The magnifying detail of experiment, (**c**) Schematic view of the SBS test specimen

Figure 3(c) shows the schematic view of the experimental setup according to the ASTM D2344 standard [34] which is for the short-beam strength of polymer matrix composite materials. The SBS specimens did not include any pre-crack using Teflon film. The span-to-thickness ratio was set to four. The length-to-thickness ratio and width-to-thickness ratio were set to six and two, respectively.

The ILSS was calculated using the classical beam theory (Bernoulli–Euler), and the maximum shear stress acting on the beam section in SBS tests was estimated as [34]:

$$\tau = 0.75\frac{P_m}{w \cdot t} \tag{1}$$

where P_m was the applied maximum or failure load, τ was the ILSS, w and t were the width and thickness of specimen, respectively.

3.2 Double Cantilever Beam (DCB) Test

Mode I fracture toughness was obtained by performing DCB tests according to the ASTM D5528-01 standard [35]. A total of two DCB specimens were prepared for each RT, 50C and 80C test. The DCB test configuration is shown in Fig. 4(a). The specimens were loaded in a servohydraulic Instron 8500 universal testing machine equipped with a 200 N force cell. The loading rate used in DCB tests was determined as 1.2 mm/min based on the ASTM D5528-01 standard which stated that a constant displacement rate in the range from 0.5 to 5.0 mm/min can be used. One end of the specimen was fixed on the fixture. The delamination crack length was obtained from a traveling recording camera of each test, which was recorded at ~ 1000 frames per second.

Figure 4(b) shows the schematic image of DCB specimen under the exerted load *P*, the displacement δ and the delamination length (x) which was measured along the horizontal direction. The specimen was glued to the metal blocks as shown in Fig. 4(c). The overall geometry and the dimensions of the DCB specimen are illustrated in Fig. 4(d). The length of the teflon insert and the initial crack (a_0) were 55 mm ± 2 mm and 48 mm ± 2 mm, respectively.

The modified beam theory was applied to evaluate the strain energy release rate (SERR) in Mode-I with the correction factors for large displacement [35] as:

$$G_{IC} = \frac{3P\delta}{2w(x + |\Delta|)}\left(\frac{F}{N}\right) \tag{2}$$

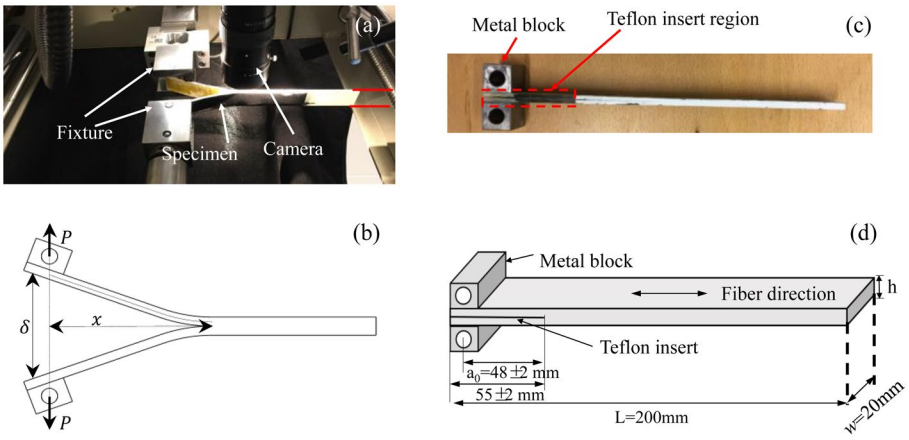

Fig. 4 (**a**) DCB test setup. (**b**) Schematic illustration of a DCB specimen undergoing large displacement, (**c**) The painted specimen with metal blocks, (**d**) The geometry of DCB specimen

where P was the critical force, δ was the displacement, x was crack tip location as defined in Fig. 4(b), w was the width of the specimen (mm), Δ was the correction factor for the rotation of the beam at the crack tip, N was the correction factor for the loading blocks and F was the correction factor for the large-displacement [35]. Since the delamination length was measured using the horizontal position of the traveling camera system, there was no need for a large-displacement correction factor. Therefore, F was set to 1 as was also done in [36].

The interlaminar fracture toughness was calculated based on the SERR for Mode-I (G_{IC}) both for initiation and propagation. The initiation values of ($G_{IC\text{-}I}$) were determined corresponding to the load and displacement for the first point at which the delamination was visually observed to grow from the insert edge using the microscope [35]. As shown in [37], when unstable crack propagation occurs, the crack propagation values, $G_{IC\text{-}P}$, can be obtained from the successive values of the critical load P just prior to crack instability.

3.3 End Notched Flexure (ENF) Test

The mode-II interlaminar fracture (G_{IIC}) was obtained by performing the end notched flexure (ENF) test. The tests were carried out according to ASTM D7905M-14 standard [38] by utilizing the Zwick/Z100 universal testing machine with an adaptation of crossheads and supporting fixtures as shown in Fig. 5. A total of five ENF specimens were prepared for each RT, 50C and 80C laminate. The loading for the ENF tests was handled by using a displacement control at a nominal rate of 0.5 mm/min [38]. The geometry of the ENF specimens was the same of DCB specimens. A total of four black lines was marked on one side of each specimen as seen in Fig. 5. The three marking lines were used for compliance calibration (CC) at different locations (i.e. a_0, a_1 and a_2). The crack tip marking line was used to identify whether the crack propagation was initiated.

The mode II interlaminar fracture toughness, G_{IIC}, was obtained by using the compliance calibration (CC) method for the non-precracked (NPC) fracture test [38]. Figure 6 shows the schematic view of the ENF experiment with its dimensions.

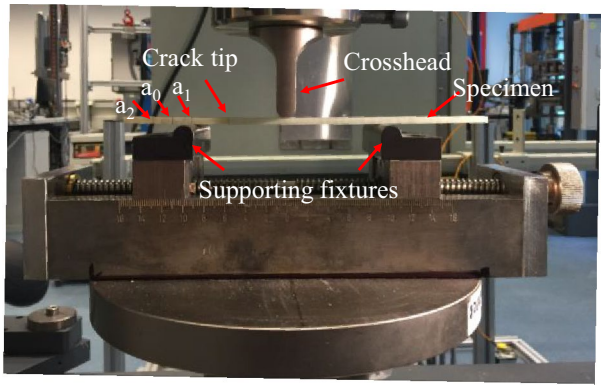

Fig. 5 The ENF test setup

According to the standard, the distance from the marks a_0, a_1 and a_2 to the crack tip were determined as 30 mm, 20 mm and 40 mm, respectively. The half-span of supports (L) was 50 mm. The radius of supports and crosshead (r) was 5 mm.

A total of three ENF tests were performed for each specimen, i.e. RT, 50C and 80C, considering the three different CC markings (a_0, a_1 and a_2). The first test was performed for $a_1 = 20$ mm in which the specimens were positioned on the 3-point bending test set up and the mark denoted as a_1 was positioned on the support center located as shown in Fig. 5. When the applied force reached to a predetermined value, at which the delamination does not start, the test was ended. The predetermined forces during ENF test are equal to 50% of the expected value of the maximum force (P_{max}) at that particular crack length [38]; Afterward, the same specimen was repositioned for $a_2 = 40$ mm and the same procedure was applied. For the last test in NPC technique, the marking denoted as $a_0 = 30$ mm was used. At this point, the ENF test was performed until the delamination was observed and the test was stopped when the measured force value reached its maximum value.

The obtained load–displacement data was useful to calculate the parameters, the compliances and compliance calibration (CC) coefficients, for obtaining the G_{IIC} [38]. The compliance equation (seen in Eq. 3) was established by using the experimental data to predict the crack length. The CC coefficients in Eq. 3, i.e. A and m, were determined from the linear regression analysis of the measured Compliance (C) and crack length cubed (a^3) [38].

$$C = A + ma^3 \tag{3}$$

Accordingly, G_{IIC} can be obtained as [38]:

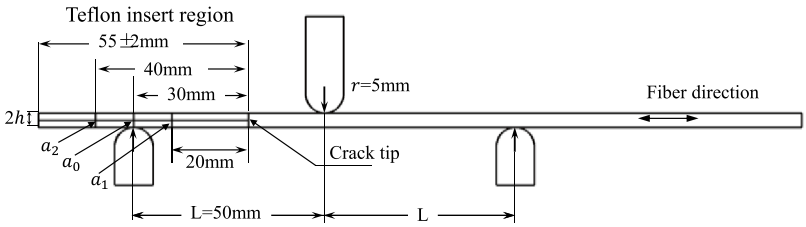

Fig. 6 The schematic view of the ENF test setup with the dimensions

$$G_{IIC} = \frac{3mP_{max}^2 a_0^2}{2B} \tag{4}$$

where P_{max} was the maximum force that initiated the delamination, a_0 was the crack length to start the delamination, i.e. $a_0 = 30$ mm, m was the constant used for the compliance in Eq. 3 and B was the specimen width.

The mode II fracture surfaces of Elium®150 composites were examined with SU8200 scanning electron microscopes (SEM). Prior to examination, the fracture surfaces were sputter-coated with a thin evaporated layer of gold for a period of 5 min. The objective of the SEM examination was to analyze the failure by studying delamination fractography, especially on bonding strength at the fiber/matrix interface. Since the fracture surface of mode I has many similarities to the fracture surface of mode II [39], only the fracture surface of mode II was analyzed in this work. The SEM examinations were concentrated on the area where the force was measured.

4 Results

4.1 Temperature Evolution and Microstructure

Figure 7 shows the temperature evolution of the RT, 50C and 80C laminates during the manufacturing process. When the laminates were manufactured at room temperature (24 ℃), 50 °C and 80 °C, the peak temperatures of three laminates were measured to be approximately 48.5 °C, 85.5 °C and 95.3 °C, respectively. The experimental results indicate that the peak temperature and polymerization rate of laminates increase as the processing temperature rises. The peak temperature was mainly due to the internal heat generation coming from the exothermic reaction of the radical polymerization of Elium resins [29, 40].

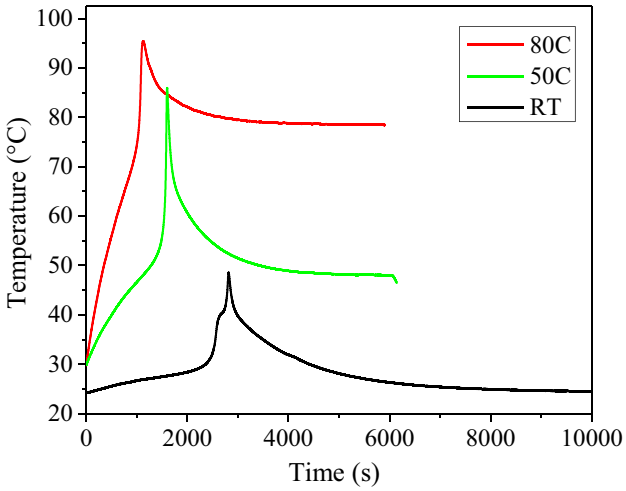

Fig. 7 The measured temperature evolution as a function of time for 80C, 50C and RT laminates

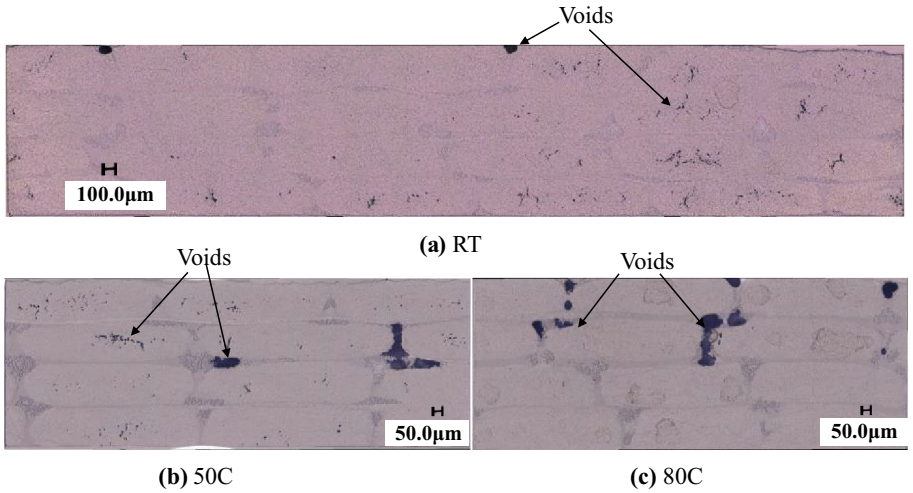

Fig. 8 Exemplary cross sections of the laminates obtained from the optical light microscopy (**a**) RT, (**b**) 50C, (**c**) 80C

The micrographs of the cross-section of the manufactured laminates are shown in Fig. 8. As seen in Fig. 8, the glass fibers were uniformly distributed in the matrix, indicating that the increase in process temperature did not affect the quality of the resin-impregnated fibers. Some voids appeared in and between the fiber bundles, and the number and size of the voids increased gradually with the increase of the process temperature. However, the void content for the three laminates was found to be below 1.5% by analyzing the microscopy images.

4.2 Interlaminar Shear Strength (ILSS)

During the SBS tests, both interlaminar shear and compressive failure were observed as seen in Fig. 9. The local stress concentrations took place at the loading nose location due to the relatively tough matrix material which resulted in compressive failure. The combined failure mode was found to exist in most of the SBS specimens. According to the video analysis during the experiment, it was noted that the interlaminar shear failure occurred just after compressive failures.

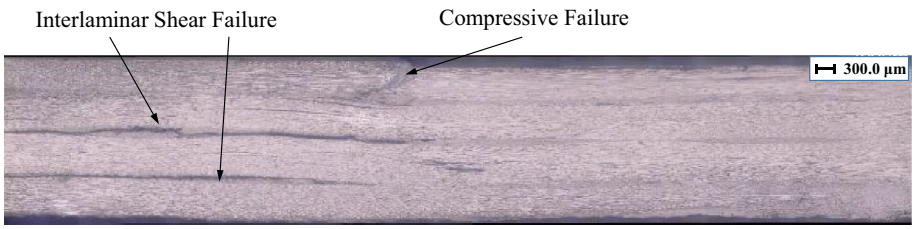

Fig. 9 Optical microscopy image of the fractured specimen after the SBS test. The interlaminar shear and compressive failure types are clearly visible

Fig. 10 Measured force–displacement response under SBS loading (left) and the camera shots for corresponding specimen (right) under three-point bending condition ▶

Figure 10 shows the experimentally obtained force–displacement curves for the RT, 50C and 80C laminates and images of the crack initiation and propagation during SBS tests. In Fig. 10(a, c) for the RT and 50C specimens, the force increases first, then flattens for a period, and finally starts decreasing. As seen in Fig. 10(e) for the 80C specimens, the force reaches the first peak, then slowly increases to the second peak, and finally decreases significantly. The compressive failures generally took place when the loads increased to the point that was approaching to the maximum force. The related behaviour of failure as a function of time is highlighted with white dashed regions in Fig. 10(b, d, f), e.g., t = 50 s, 65 s for RT specimen. The interlaminar shear failure initiated and propagated at the interface between the second and third layers as expected due to having the maximum shear stress at the neutral axis of the laminate. Further propagation of the crack resulted in a delamination. The interlaminar shear failure evolution as a function of time are highlighted with red dashed regions in Fig. 10, e.g., t = 100 s, 115 s for RT-specimen. Accordingly, the ILSS was calculated based on the force value at the delamination initiation of the specimens.

Figure 11 shows the average ILSS values of 5 specimens for each RT, 50C and 80C laminates which were approximately 50.26 MPa, 54.69 MPa and 71.18 MPa, respectively. These values were compared with the published SBS values in literature (see Table 1 for the values) as seen in Fig. 11 and it was found that the present average SBS value of the RT laminate (~ 50 MPa) is comparable with the published average SBS value (~ 48 MPa). The experimental results indicated that the increase in processing temperature resulted in an increase in the ILSS.

4.3 Mode I Fracture Toughness (G_{IC})

The measured force–displacement response and the corresponding fracture behaviour of DCB specimens are illustrated in Fig. 12(a). For all specimens, the measured force first increased linearly up to a certain point after which it increased non-linearly up to its maximum value. After the maximum force was reached, the force dropped due to the crack propagation. The unloading curve reveals that no significant permanent plastic deformation of the specimens was observed. Hence, it was assumed that the maximum crack position of approximately 3 mm after unloading at the two edges of the specimen did not influence the G_{IC} estimations [35, 41].

As shown in Fig. 12(a), two types of crack propagation behaviors, i.e. stable propagation and unstable propagation, were observed based on the force fluctuations. The stable crack propagation was the case when the crack propagated continuously with smaller fluctuations in force under the external loading. The unstable propagation was the case in which the crack was undergoing a series of rapid propagation events with larger fluctuation in force. The unstable crack propagation can be mainly explained by the plastic fracture due to the shear yielding of matrix formation in the crack-tip [7]. This behaviour always indicates that the Elium composites have strong fiber/matrix adhesion and high ductile matrix properties.

Fiber bridging was observed in all unidirectional specimens as shown in Fig. 12(b-c). Fiber filaments or fiber bundles were peeled from the matrix along the fiber direction of the specimens. This indicates that fiber-matrix debonding were the dominant damage mechanism in the specimens [42, 43]. The fiber bridging is beneficial to the fracture

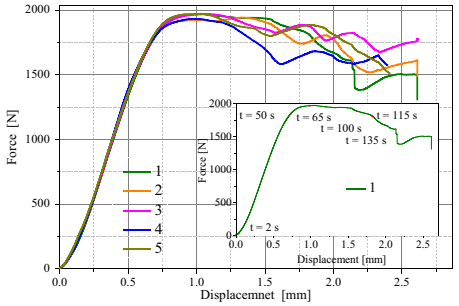

(a) Force-displacement of RT specimen.

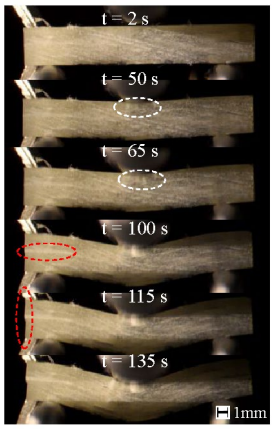

(b) Camera shots of RT specimen.

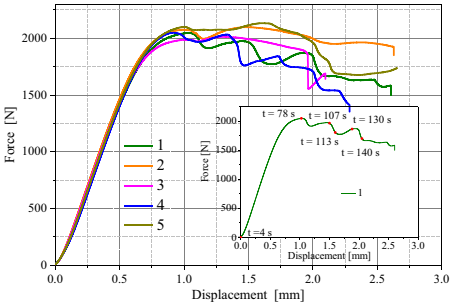

(c) Force-displacement of 50C specimen.

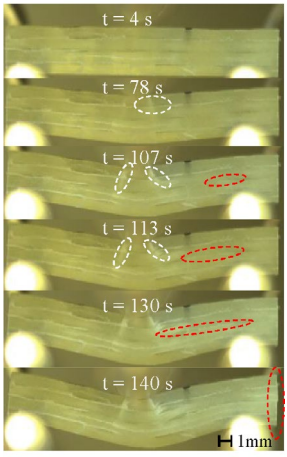

(d) Camera shots of 50C specimen.

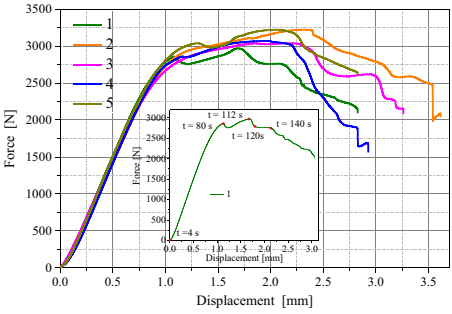

(e) Force-displacement of 80C specimen.

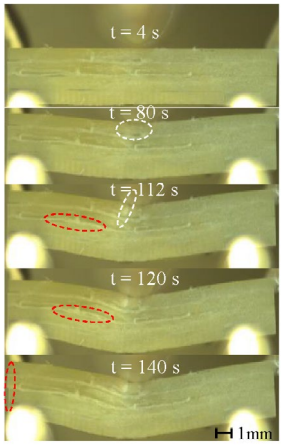

(f) Camera shots of 80C specimen.

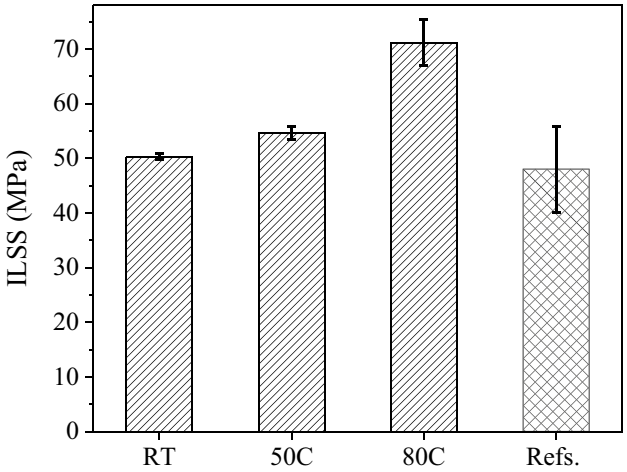

Fig. 11 The measured average ILSS with its standard deviation based on the five tests for RT, 50C and 80C laminates and the reported ILSS values in Refs. [5, 21–24]

toughness [44] and favors in higher toughness applications, which would increase the range of applications of Elium composites.

Figure 13(a) shows the experimentally obtained G_{IC} as a function of the delamination crack length (R-curves) obtained from the force–displacement response for the RT, 50C and 80C specimens. The first point of the R-curve corresponds to the initiation value for interlaminar fracture toughness. The propagation values for $G_{IC\text{-}P}$ were determined as the average of the values recorded over a wide range of crack growth where G_{IC} was in a plateau region. It can be shown that the R-curves obtained from two experiments of each laminate were similar indicating that repeatable results were obtained from the DCB tests. The slowly increasing R-curve was observed for all cases which could be caused by the fiber bridging [45]. Among three different laminates, 80C laminate showed the highest G_{IC} both at the initiation and propagation period, which could be due to the strong bonding performance between fiber and matrix.

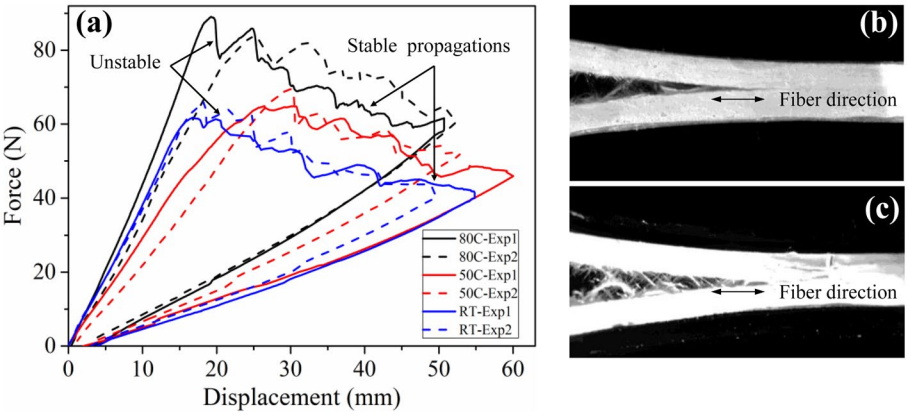

Fig. 12 (**a**) Two DCB load–displacement curves for each 80C, 50C, RT laminates; Typical fiber bridging of the 80C laminate for the different displacement: (**b**) displacement = 20 mm, (**c**) displacement = 33 mm

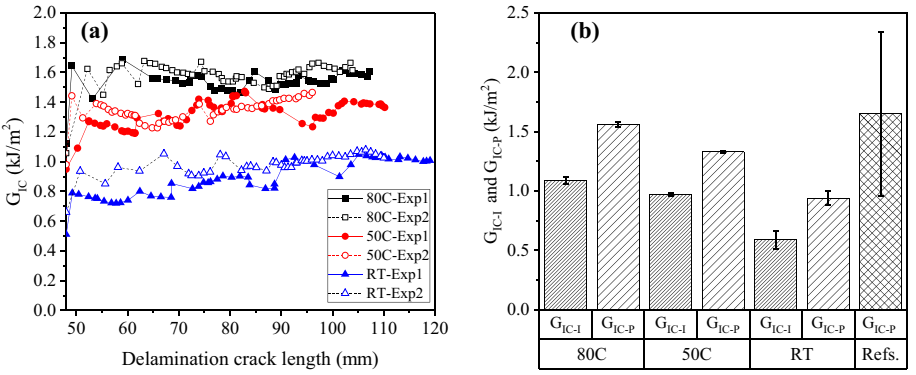

Fig.13 (**a**) R-curves for RT, 50C and 80C laminates, two data sets for each case. (**b**) The comparison of G_{1C-I} and G_{1C-P} (average with standard deviation) values for different types laminate as well as average G_{1C-P} values reported in Refs [5, 7, 24–26]

The average G_{IC-I} and G_{IC-P} for two specimens from RT, 50 ℃ and 80 ℃ laminates as well as the average G_{IC-P} obtained from Refs. [5, 7, 24–26] are shown in Fig. 13(b). The average G_{IC-I} of 80C laminates was found to be approximately 1.09 kJ/m^2, which was higher than those of the 50C laminate (G_{IC-I}=0.97 kJ/m^2) and RT laminate (G_{IC-I}=0.59 kJ/m^2). This indicates that the initial fracture toughness can be improved by increasing the processing temperature. Similarly, the fracture toughness (G_{IC-P}) was increased by 66% (from 0.94 kJ/m^2 to 1.56 kJ/m^2) when the processing temperature increased from room temperature to 80 ℃. While for the 50C specimen, the G_{IC-P} value increased by 41% as compared with the RT specimen (from 0.94 kJ/m^2 to 1.33 kJ/m^2). The average G_{IC-P} obtained from the Refs. was approximately 1.65 kJ/m^2 which was found to be close to the G_{IC-P} range obtained in this work.

4.4 Mode II Fracture Toughness (G_{IIC})

The force–displacement responses of the laminates (RT, 50C and 80C) in the ENF tests are depicted in Fig. 14. A gradual decrease in the force with respect the crack growth was found to be the case for the 50C and 80C specimens indicating a stable delamination progression. On the other hand, the RT specimens had a sharp drop in force during the crack growth which was due to the unstable delamination.

The fracture toughness parameters of RT, 50C and 80C laminates are shown in Tables 2, 3 and 4. The maximum force (P_{max}), width (B) and Compliances (a_1=20, a_0=30, a_2=40) were obtained from experiments. The parameter B of all specimens was found to be approximately 20 mm. The standard deviation (S.D.) of P_{max} was calculated approximately as 146 N, 111 N and 67 N for five RT specimens, four 50C samples and five 80C specimens, respectively. The possible reasons for these variations in the obtained Pmax were i) the variation in the local fiber distributions and potential voids within the specimens, ii) the inherent measurement errors and iii) the local large deformations at the onset of precipitation growth affecting the accuracy of the ENF test results [38, 46]. The CC coefficient (m) was determined using a linear least squares linear regression analysis of the compliance C versus crack length cubed a^3. Figure 15 shows a linear fit to the average data points of NPC tests for three different laminates, i.e. RT, 50C and 80C. The relationship

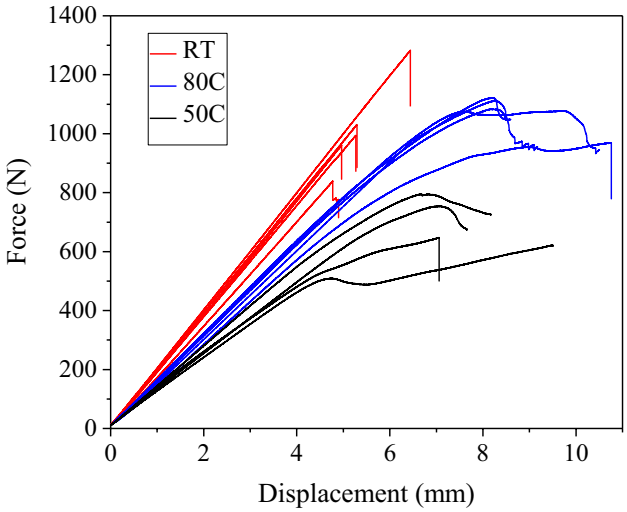

Fig. 14 Force–displacement response in ENF tests

between the compliance and crack length was analyzed according to ASTM D7905M-14 standard. These parameters (B, P_{max} and m) were used to determine G_{IIC} according to Eq. 4.

The average and standard deviation of the G_{IIC} values for each case are shown in Fig. 16 together with the reported the G_{IIC} in the literature [27]. It is seen that the G_{IIC} of RT laminate is in the same order of magnitude as the reported G_{IIC} in the literature. When the processing temperature was increased from room temperature to 50 ℃ and 80 ℃, the G_{IIC} increased from 0.91 kJ/m^2 to 2.14 kJ/m^2 and 2.98 kJ/m^2, respectively. The increase in processing temperature improves the physical and chemical bonding between the fibre surface and the resin, thereby increasing the interfacial bonding strength and strengthening the mechanical properties of the composite.

Figure 17 illustrates the interlaminar shear fracture morphology of Elium laminates manufactured at room temperature (24 °C), 50 °C and 80 °C. As a typical Mode II failure feature, cusps were found between adjacent fibers in three laminates, especially in the resin-rich regions, which were shallow and irregular. As seen in Fig. 17(a), a severe debonding of matrix from the fibers was visible for the RT laminate, indicating that the adhesion of the fiber-matrix interface was poor and a shear damage originated from interfacial debonding.

Table 2 Parameters and G_{IIC} obtained during the NPC fracture tests for RT laminate

Test	Specimen	B(mm)	P_{max} (N)	C(mm/N)			m 1/(Nmm^2)	G_{IIC} kJ/m^2
				$a_1 = 20$ mm	$a_0 = 30$ mm	$a_2 = 40$ mm		
RT	1	1.96E+01	9.61E+02	4.89E-03	5.18E-03	5.66E-03	1.35E-08	0.86
	2	1.97E+01	1.28E+03	4.90E-03	5.04E-03	5.52E-03	1.13E-08	1.27
	3	1.97E+01	9.94E+02	5.32E-03	5.33E-03	5.87E-03	1.04E-08	0.71
	4	1.96E+01	8.39E+02	5.22E-03	5.71E-03	6.12E-03	1.55E-08	0.75
	5	1.97E+01	1.03E+03	5.05E-03	5.16E-03	5.75E-03	1.29E-08	0.94
Average		1.97E+01	1.02E+03	5.08E-03	5.28E-03	5.78E-03	1.27E-08	0.91
S.D		4.31E-02	1.46E+02	1.72E-04	2.30E-04	2.06E-04	1.78E-09	0.2

Table 3 Parameters and G_{IIC} obtained during the NPC fracture tests for 50C laminate

Test	Specimen	B(mm)	P_{max} (N)	C(mm/N)			m $1/(Nmm^2)$	G_{IIC} kJ/m^2
				$a_1 = 20$ mm	$a_0 = 30$ mm	$a_2 = 40$ mm		
50C	1	2.05E+01	6.46E+02	5.92E-03	8.90E-03	9.85E-03	6.52E-08	1.77
	2	2.05E+01	7.53E+02	5.93E-03	8.30E-03	9.91E-03	6.74E-08	2.52
	3	2.03E+01	5.08E+02	5.92E-03	8.91E-03	1.03E-02	7.25E-08	1.24
	4	2.02E+01	7.94E+02	5.89E-03	7.42E-03	9.96E-03	7.22E-08	3.04
Average		2.04E+01	6.75E+02	5.91E-03	8.38E-03	1.00E-02	6.93E-08	2.14
S.D		1.08E-01	1.11E+02	1.55E-05	6.09E-04	1.72E-04	3.11E-09	0.69

As a result, the energy needed for crack propagation and hence G_{IIC} for RT laminate were affected adversely [39]. In contrast, no matrix debonding was observed for the 50C and 80C laminate as seen in Fig. 17(b) and (c), respectively. This indicates that a better fiber-matrix adhesion was present for 50C and 80C laminates than the RT laminate. It should be noted that the surface area of the fibers that were covered by the matrix residue after the fracture was quantitatively found to be larger in 80C laminate than 50C laminate as seen in Fig. 17(b) and (c). This resulted in a better fiber-to-resin adhesion for the 80C laminate than that of the 50C laminate. A ductile matrix failure between two adjacent fibers can be observed for the 50C and 80C laminate as seen in Fig. 17(b) and (c) which illustrates that the matix undergoes deformation in order to prevent shear failure when damage occurs. The aforementioned morphological observations based on the SEM images in Fig. 17 clearly reflect the effect of process temperature on the adhesion between the fiber and resin.

5 Discussion

Table 5 summarizes the tests results obtained for glass/Elium laminates that were formed at different processing temperatures. The performed SBS, DCB and ENF tests were found to be repeatable based on the relatively low standard deviations obtained as seen in Table 5. When the processing temperature increased form 24 ℃ to 80 ℃, the interlaminar shear strength, Mode I and Mode II interlaminar fracture toughness was improved by approximately 41%, 66% and 227%, respectively. The peak temperature of the laminate during the polymerization process was higher than the set temperature due to internal heat generation which resulted in a different polymerization rates which can be interpreted from the heating rates seen in Fig. 7. As it is known and showed also in [47–49] that the processing history

Table 4 Parameters and G_{IIC} obtained during the NPC fracture tests for 80C laminate

Test	Specimen	B(mm)	P_{max} (N)	C(mm/N)			m $1/(Nmm^2)$	G_{IIC} kJ/m^2
				$a_1 = 20$ mm	$a_0 = 30$ mm	$a_2 = 40$ mm		
80C	1	1.96E+01	9.54E+02	5.48E-03	6.95E-03	7.78E-03	3.85E-08	2.41
	2	1.97E+01	1.12E+03	5.05E-03	6.35E-03	7.04E-03	3.31E-08	2.85
	3	1.96E+01	1.08E+03	5.27E-03	6.38E-03	7.62E-03	4.07E-08	3.26
	4	1.96E+01	1.08E+03	5.19E-03	6.52E-03	7.39E-03	3.70E-08	2.99
	5	1.97E+01	1.11E+03	5.49E-03	6.80E-03	7.83E-03	3.99E-08	3.38
Average		1.96E+01	1.07E+03	5.30E-03	6.60E-03	7.53E-03	3.79E-08	2.98
S.D		5.72E-02	6.66E+01	1.87E-04	2.64E-04	3.25E-04	3.00E-09	0.38

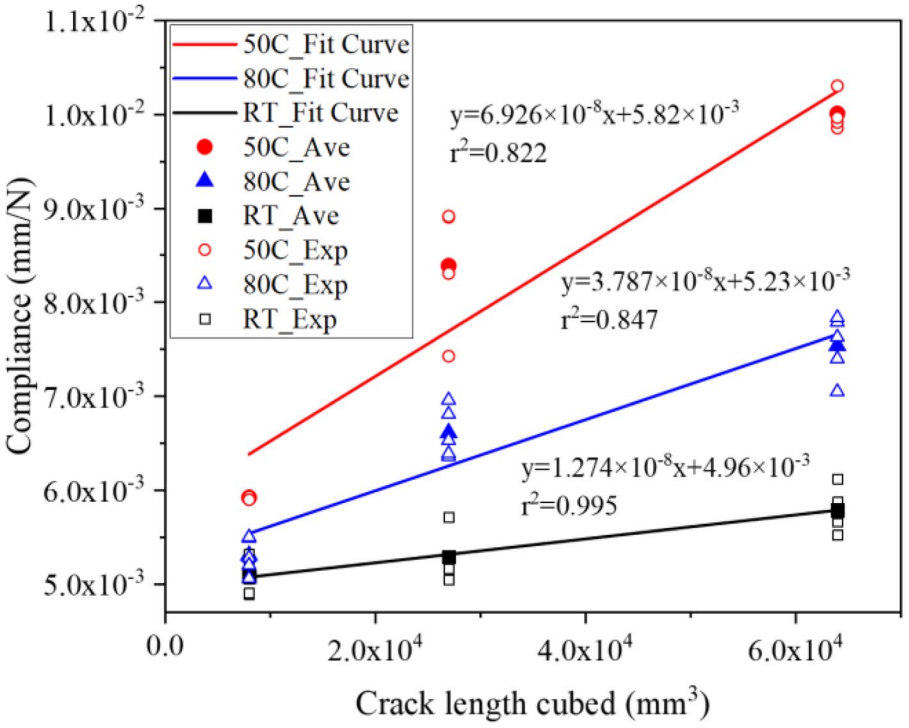

Fig. 15 Compliance versus crack cubed length for different laminates in NPC tests

and the curing path of the matrix material have an effect on the mechanical properties of the produced parts. It was shown in [48] that faster exothermic reaction of T800H/3900–2 carbon fiber reinforced polymer composites resulted in a larger G_{IC} which was also the case in the present work. This may be due to the increase of polymerization rate of Elium resin with the increase of processing temperature, which leads an increase in the matrix

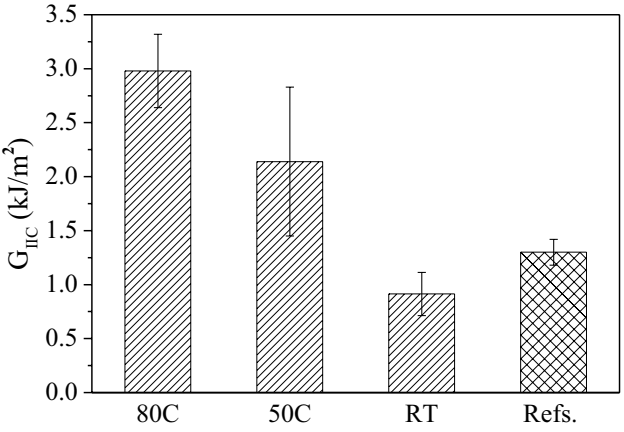

Fig. 16 The G_{IIC} of the RT, 50C and 80C laminates as well as the reported G_{IIC} in literature Refs. [27]

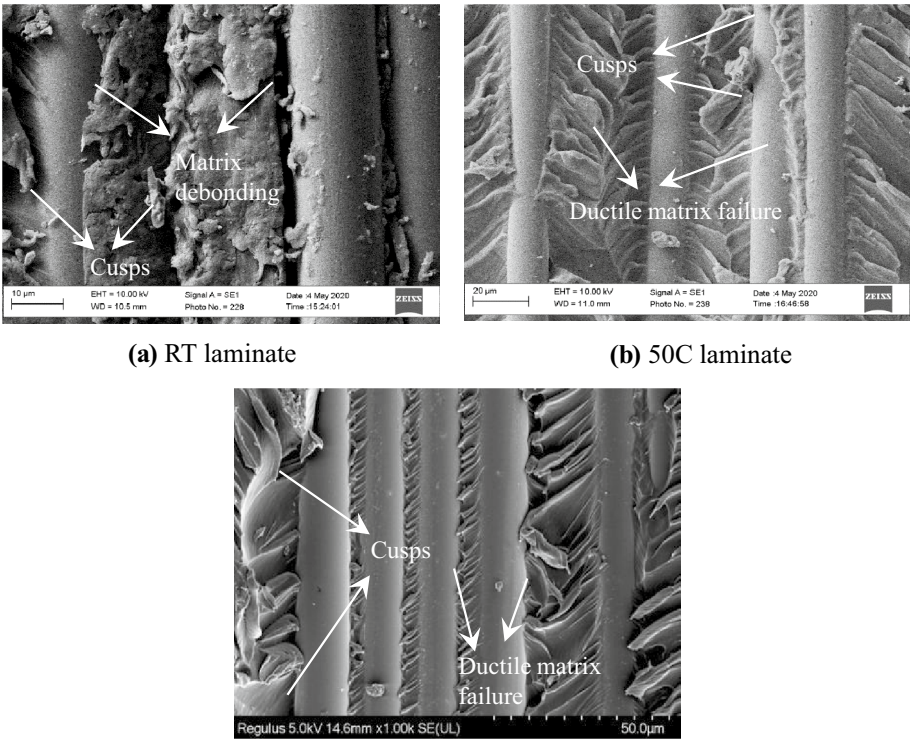

(a) RT laminate

(b) 50C laminate

(c) 80C laminate

Fig. 17 The SEM images of the mode II interlaminar fracture surface for the different laminates, (**a**) RT laminate, (**b**) 50C laminate, (**c**) 80C laminate

toughness, thereby an increase in the composite resistance against interlaminar failure [49, 50]. The processing temperature also directly affects the microscale interlaminar failure mode, i.e. adhesive failure at the fiber-matrix interface, cohesive failure in the matrix or at the fiber-matrix interphase and combined adhesive/cohesive failure. It was shown in [50] that as-moulded specimen showed areas of both interfacial and matrix failure, whereas the post-cured specimen had matrix failure only. Similarly, as shown in Fig. 17, higher processing temperature resulted in a better fiber-matrix bonding which was interpreted by analyzing the fiber surface area covered with the matrix residuals qualitatively.

Table 5 Summary of the test results of unidirectional glass/Elium composite specimens. The values in parenthesis indicate the standard deviation

Specimen	Processing Temp [℃]	Peak Temp [℃]	ILSS[MPa]	G_{IC} [kJ/m^2]		G_{IIC} [kJ/m^2]
				Init	Prop	
RT	24	48.5	50.26(0.56)	0.59(0.08)	0.94(0.06)	0.91(0.2)
50C	50	85.5	54.69(1.17)	0.97(0.02)	1.33(0.01)	2.14(0.69)
80C	80	95.3	71.18(4.21)	1.09(0.03)	1.56(0.02)	2.98(0.38)

6 Conclusions

The glass/Elium® 150 laminates were manufactured by using VARTM under three different processing temperatures: Room Temperature (24 ℃), 50 ℃ and 80 ℃. The ILSS, G_{IC} and G_{IIC} of the laminates were determined by performing the SBS, DCB and ENF test, respectively to reveal the effect of process temperature on the interlaminar behavior. The following conclusions can be drawn:

(1) The average ILSS for each RT, 50C and 80C laminates were found to be approximately 50.26 MPa, 54.69 MPa and 71.18 MPa, respectively. Camera shots showed that there was a combined compressive and interlaminar shear failure in SBS tests.
(2) The fracture toughness value was found to increase by 66% (from 0.94 kJ/m^2 to 1.56 kJ/m^2) as the processing temperature increased from room temperature to 80 ℃. Fiber bridging was present in each DCB test according to camera observations.
(3) As the processing temperature was increased from room temperature to 50 ℃ and 80 ℃, the G_{IIC} increased from 0.91 kJ/m^2 to 2.14 kJ/m^2 and 2.98 kJ/m^2, respectively. SEM images of the fracture surfaces obtained after the ENF tests showed that there was a severe matrix debonding for the RT laminate.

In general, an increase in the processing temperature resulted in an increase in ILSS, G_{IC} and G_{IIC}. A post polymerization step with a higher temperature than the processing temperature is considered as future work to isolate the effect of final polymerization degree on the interlaminar failure behavior. In order to interpret the quantitative relationship between the processing history and interfacial failure modes, a micromechanical surface characterization after the fracture tests could be performed by using an atomic force microscopy or a nanoindentation tester.

Data Availability The datasets generated during and/or analysed during the current study are available from the corresponding author on reasonable request.

References

1. Shuaib, N.A., Mativenga, P.T.: Energy demand in mechanical recycling of glass fibre reinforced thermoset plastic composites. J. Clean. Prod **120**, 198–206 (2016)
2. Bhudolia, S.K., Gohel, G., Joshi, S.C., et al.: Manufacturing Optimization and Experimental Investigation of Ex-situ Core-shell Particles Toughened Carbon/Elium® Thermoplastic Composites[J]. Fiber Polym **22**(6), 1693–1703 (2021)
3. Raponi, O.A., Barbosa, L.C.M., de Souza, B.R., et al.: Study of the influence of initiator content in the polymerization reaction of a thermoplastic liquid resin for advanced composite manufacturing. Adv Polym Tech **37**(8), 3579–3587 (2018)
4. Murray, J.J., Robert, C., Gleich, K., McCarthy, E.D., Ó Brádaigh, C.M.: Manufacturing of unidirectional stitched glass fabric reinforced polyamide 6 by thermoplastic resin transfer moulding. Mater. Des **189**, 108–512 (2020)
5. Obande, W., Mamalis, D., Ray, D., Yang, L., Brádaigh, C.M.: Mechanical and thermomechanical characterisation of vacuum-infused thermoplastic- and thermoset-based composites. Mater Des **175**, 107–828 (2019)
6. Murray, R.E., Penumadu, D., Cousins, D., Beach, R., Snowberg, D., Berry, D., Stebner, A.: Manufacturing and Flexural Characterization of Infusion-Reacted Thermoplastic Wind Turbine Blade Subcomponents. Appl Compos Mater **26**(3), 945–961 (2019)

7. Shanmugam L, Kazemi M, Rao Z, Lu D, Wang X, Wang, B, et al.: Enhanced Mode I fracture toughness of UHMWPE fabric/thermoplastic laminates with combined surface treatments of polydopamine and functionalized carbon nanotubes. Compos B Eng **178**, 107450 (2018)
8. Zoller, A., Escalé, P., Gérard, P.: Pultrusion of Bendable Continuous Fibers Reinforced Composites With Reactive Acrylic Thermoplastic ELIUM® Resin. Front Mater **6**(13), 1–9 (2019)
9. Matadi Boumbimba, R., Coulibaly, M., Khabouchi, A., Kinvi-Dossou, G., Bonfoh, N., Gerard, P.: Glass fibres reinforced acrylic thermoplastic resin-based tri-block copolymers composites: Low velocity impact response at various temperatures. Compos. Struct. **160**, 939–951 (2017)
10. Bhudolia, S.K., Gohel G., Kantipudi, J, et al.: Manufacturing and investigating the load, energy and failure attributes of thin ply carbon/Elium® thermoplastic hollow composites under low-velocity impact. Mater Design **206**, 109814 (2021)
11. Gohel, G., Bhudolia, S.K., Subramanyam, E.S.B, et al.: Development and impact characterization of acrylic thermoplastic composite bicycle helmet shell with improved safety and performance. Compos Part B: Eng 109008 (2021)
12. Bhudolia, S.K., Gohel, G., Kantipudi, J, et al.: Mechanical performance and damage mechanisms of thin rectangular carbon/Elium® tubular thermoplastic composites under flexure and low-velocity impact. Thin-Walled Struct **165**, 107971 (2021)
13. Bhudolia, S.K., Joshi, S.C., Bert, A., Di Yi, B., Makam, R., Gohel, G.: Flexural characteristics of novel carbon methylmethacrylate composites. Compos. Commun. **13**, 129–133 (2019)
14. Bhudolia, S.K., Joshi, S.C., Boon, Y.D.: Experimental and Microscopic Investigation on Mechanical Performance of Textile Spread-tow Thin Ply Composites. Fibers Polym. **20**, 1036–1045 (2019)
15. Haggui, M., EL Mahi, A., Jendli, Z., Akrout, A., Haddar, D.: Damage Analysis of Flax Fibre/Elium Composite Under Static and Fatigue Testing. International Conference Design & Modeling of Mechanical Systems. Springer, Cham (2017)
16. Chilali, A., Zouari, W., Assarar, M., Kebir, H., Ayad, R.: Analysis of the mechanical behaviour of flax and glass fabrics-reinforced thermoplastic and thermoset resins. J REINF PLAST COMP **35**(16), 1217–1232 (2016)
17. Haggui, M., El Mahi, A., Jendli, Z., Akrout, A., Haddar, M.: Static and fatigue characterization of flax fiber reinforced thermoplastic composites by acoustic emission. Appl. Acoust. **147**(4), 100–110 (2018)
18. Bhudolia, S.K., Gohel, G., Fai, L.K., Barsotti, R.J.: Fatigue response of ultrasonically welded carbon/elium® thermoplastic composites. Mater Lett **264**, 127362 (2020)
19. Cadieu, L., Kopp, J.B., Jumel, J., Bega, J., Froustey, C.: Temperature effect on the mechanical properties and damage mechanisms of a glass/thermoplastic laminate. J Compos Mater **54**(17), 002199831989438 (2019)
20. Cadieu, L., Kopp, J.B., Jumel, J, et al.: Strain rate effect on the mechanical properties of a glass fibre reinforced acrylic matrix laminate. An experimental approach. Compos Struct **223**,110952 (2019)
21. Nash, N.H., Portela, A., Bachour, C., Manolakis, I., Comer, A.J.: Effect of environmental conditioning on the properties of thermosetting- and thermoplastic-matrix composite materials by resin infusion for marine applications. Compos B Eng **177**, 107271 (2019)
22. Bhudolia, S.K., Perrotey, P., Joshi, S.C.: Optimizing polymer infusion manufacture for thin ply textile composites with novel matrix system. Materials **10**(3), (2017)
23. Davies, P., Arhant, M.: Fatigue Behaviour of Acrylic Matrix Composites: Influence of Seawater. Appl Compos Mater **26**(2), 507–518 (2019)
24. Mamalis, D., Obande, W., Koutsos, V., Blackford, J.R., Ó Brádaigh, C.M., Ray, D.: Novel thermoplastic fibre-metal laminates manufactured by vacuum resin infusion: The effect of surface treatments on interfacial bonding. Mater Des **162**, (2019)
25. Pini, T., Caimmi, F., Briatico-Vangosa, F., Frassine, R., Rink, M.: Fracture initiation and propagation in unidirectional CF composites based on thermoplastic acrylic resins. Eng Fract Mech **184**, 51–58 (2017)
26. Bhudolia, S.K., Perrotey, P., Joshi, S.C.: Mode I fracture toughness and fractographic investigation of carbon fibre composites with liquid Methylmethacrylate thermoplastic matrix. Compos. Part B Eng. **134**, 246–253 (2018)
27. Barbosa, L.C.M.; Bortoluzzi, D.B.; Ancelotti, A.C.: Analysis of fracture toughness in mode II and fractographic study of composites based on Elium®150 thermoplastic matrix. Compos. Part B Eng **175**, 107082 (2019)
28. Baran, I., Warnet, L.L., Akkerman, R.: Assessment of failure and cohesive zone length in co-consolidated hybrid C/PEKK butt joint. Eng. Struct. **168**, 420–430 (2018)

29. Han, N., Baran, I., Zanjani, J.S.M., Yuksel, O., An, L.L., Akkerman, R.: Experimental and computational analysis of the polymerization overheating in thick glass/Elium® acrylic thermoplastic resin composites, Compos. Part B Eng **202**, (2020)
30. de Andrade Raponi, O., Righetti de Souza, B., Miranda Barbosa, L.C., Ancelotti Junior, A.C.: Thermal, rheological, and dielectric analyses of the polymerization reaction of a liquid thermoplastic resin for infusion manufacturing of composite materials. Polym Test **71**(8), 32–37 (2018)
31. Su-jin, Kim., Jinho Jang.: Effect of degree of polymerization on the mechanical properties of regenerated cellulose fibers using synthesized 1-allyl-3-methylimidazolium chloride. Fiber Polym (2013)
32. Balani, K., Verma, V., Agarwal, A., Narayan, R.: Physical, Thermal, and Mechanical Properties of Polymers. Biosurfaces. John Wiley & Sons, Ltd. (2015)
33. Demircan, G., Kisa, M., Ozen, M., et al.: Surface-modified alumina nanoparticles-filled aramid fiber-reinforced epoxy nanocomposites: preparation and mechanical properties. Iran Polym J **29**, 253–264 (2020)
34. ASTM D2344 / D2344M - 16.: Standard Test Method for Short-Beam Strength of Polymer Matrix Composite Materials and Their Laminates, ASTM Int., (2016)
35. ASTM D5528–01.: Standard Test Method for Mode I Interlaminar Fracture Toughness of Unidirectional Fiber-Reinforced Polymer Matrix Composites. ASTM International: West Conshohocken, P.A
36. ISO 15024.: Standard Test Method for Mode I interlaminar Fracture Toughness, G_{IC}, of Unidirectional Fibre-reinforced Polymer Matrix Composites, (1997)
37. Perrin F, Bureau M N, Denault, J, et al. Mode I interlaminar crack propagation in continuous glass fiber/polypropylene composites: Temperature and molding condition dependence. Compos Sci Technol **63**(5), 597–607 (2003)
38. ASTM D7905/D7905M-14.: Standard Test Method for Determination of the Mode II Interlaminar Fracture Toughness of Unidirectional Fiber-Reinforced Polymer Matrix Composites, ASTM International, West Conshohocken (2014)
39. Zhao, X., Chen, W., Han, X., Zhao, Y., Du, S.: Enhancement of interlaminar fracture toughness in textile-reinforced epoxy composites with polyamide 6/graphene oxide interlaminar toughening tackifier. Compos Sci Technol **191**(2), (2020)
40. Hwan Shin, J., Kim, D., Centea, T., Nutt, S.R.: Thermoplastic prepreg with partially polymerized matrix: material and process development for efficient part manufacturing. Compos Part A: Appl Sci Manufac (2019)
41. Sacchetti, F., Grouve, W., Warnet, L.L, et al.: Interlaminar fracture toughness of 5HS Carbon/PEEK laminates. A comparison between DCB, ELS and mandrel peel tests. Polym Test **66**, 13–23 (2018)
42. Li, Y., Liu, X., Chen, G., Ren, C.: Study on interfacial debonding stress and damage mechanisms of C/SiC composites using acoustic emission. Ceram. Int. **47**(4), 4512–4520 (2021)
43. Sacchetti, F., Wouter, J.B., Grouve, L.L., Villegas, W.I.F.: Effect of cooling rate on the interlaminar fracture toughness of unidirectional Carbon/PPS laminates. Eng Fract Mech **203**, 126–136 (2018)
44. Rafiullah, K.: Fiber bridging in composite laminates: A literature review, Composite Structures **229**, 111418,ISSN 0263–8223 (2019)
45. Sacchetti, F., Grouve, W.J., Warnet, L.L., Villegas, I.F.: Effect of cooling rate on the interlaminar fracture toughness of unidirectional Carbon/PPS laminates. Eng Fract Mech **203**, 126–136 (2018)
46. Rzeczkowski, J.: An experimental analysis of the end-notched flexure composite laminates beams with elastic couplings. Continuum Mech. Thermodyn. **33**, 2331–2343 (2021)
47. Hunt, C., Kratz, J., Partridge, I.K.: Cure path dependency of mode I fracture toughness in thermoplastic particle interleaf toughened prepreg laminates. Compos. A **87**, 109–114 (2016)
48. Zhang, J., Fox, B.L.: Manufacturing influence on the delamination fracture behavior of the T800H/3900-2 carbon fiber reinforced polymer composites. Mater Manuf Process **22**, 768–772 (2007)
49. Tucker, R., Compston, P., Jar, P.Y.: The effect of post-cure duration on the mode I interlaminar fracture toughness of glass-fibre reinforced vinylester. Compos. A Appl. Sci. Manuf. **32**(1), 129–134 (2001)
50. Lindsey, K.A., Rudd, C.D., Fraser, I.M.: Effects of post-cure on the interfacial properties of glass fibre-urethane methacrylate composites. J. Mater. Sci. Lett. **12**(12), 894–897 (1993)